

**Seawater Electrolysis**

# High-Performance Alkaline Seawater Electrolysis with Anomalous Chloride Promoted Oxygen Evolution Reaction

Hao Liu<sup>+</sup>, Wei Shen<sup>+</sup>, Huanyu Jin, Jun Xu, Pinxian Xi, Juncai Dong,\* Yao Zheng,\* and Shi-Zhang Qiao\*

**Abstract:** A highly selective and durable oxygen evolution reaction (OER) electrocatalyst is the bottleneck for direct seawater splitting because of side reactions primarily caused by chloride ions ( $\text{Cl}^-$ ). Most studies about OER catalysts in seawater focus on the repulsion of the  $\text{Cl}^-$  to reduce its negative effects. Herein, we demonstrate that the adsorption of  $\text{Cl}^-$  on the specific site of a popular OER electrocatalyst, nickel-iron layered double hydroxide (NiFe LDH), does not have a significant negative impact; rather, it is beneficial for its activity and stability enhancement in natural seawater. A set of in situ characterization techniques reveals that the adsorption of  $\text{Cl}^-$  on the desired Fe site suppresses Fe leaching, and creates more OER-active Ni sites, improving the catalyst's long-term stability and activity simultaneously. Therefore, we achieve direct alkaline seawater electrolysis for the very first time on a commercial-scale alkaline electrolyser (AE, 120  $\text{cm}^2$  electrode area) using the NiFe LDH anode. The new alkaline seawater electrolyser exhibits a reduction in electricity consumption by 20.7% compared to the alkaline purified water-based AE using commercial Ni catalyst, achieving excellent durability for 100 h at 200  $\text{mA cm}^{-2}$ .

## Introduction

Water electrolysis has attracted intensive interest in producing pure hydrogen.<sup>[1]</sup> Currently, most types of water electrolyzers, either mature AE or emerging proton exchange membrane (PEM)-based water electrolysis technology, require the supply of water with low impurity concentration (e.g. deionized water) as feedstock.<sup>[2,3]</sup> As a result, large-scale water splitting in the future will need a large amount of freshwater resources.<sup>[4]</sup> A route to alleviate water scarcity caused by increased water usage for electrolysis would be to use (almost) infinite seawater as the water feedstock. However, the application of seawater electrolysis is hindered by its complex composition, such as major  $\text{Cl}^-$  ( $\approx 0.55$  M), sodium ions ( $\text{Na}^+$ ,  $\approx 0.48$  M), magnesium ions ( $\text{Mg}^{2+}$ ,  $\approx 0.05$  M), etc (Figure S1).<sup>[5]</sup> Specifically, on the anode, the chlorine evolution reaction (CIER) can compete with the oxygen evolution reaction (OER) due to their similar thermodynamic equilibrium potentials and faster kinetics reaction rate of CIER.<sup>[6,7]</sup> Thus,  $\text{ClO}^-$ , as the oxidation product of CIER in alkaline conditions, would lead to severe corrosion problems on the whole electrolyser.<sup>[8]</sup> Currently, there are two ways to realize seawater splitting: indirect seawater splitting and direct seawater splitting.<sup>[9]</sup> For indirect water splitting, the seawater is first desalinated by reverse osmosis (RO) technology before being used in a commercial electrolyser, which solves the problems of CIER and corrosion. However, taking Australia as an example, the capacity of seawater desalination will not meet the increasing demand for hydrogen production by water electrolysis (Figure S2 and Supplementary note 1).<sup>[10,11]</sup> Therefore, it is very necessary to develop direct seawater splitting by an electrolyser that uses seawater without RO treatment.<sup>[12,13]</sup> However, PEM-based water electrolyzers show extremely high sensitivity to  $\text{Cl}^-$  because of the intrinsic properties of noble metal catalysts.<sup>[14,15]</sup> Besides, although the anion exchange membrane (AEM)-based electrolyzers have preliminarily demonstrated the feasibility of seawater as the feedstock, its performance is hindered by the limited mass transfer across the membrane caused by  $\text{Cl}^-$  blocking.<sup>[16,17]</sup> To this end, the mature AE technology would be suitable for direct seawater splitting because the high pH suppresses the CIER,<sup>[18]</sup> and its asbestos diaphragm can avoid the  $\text{Cl}^-$  blockage. Meanwhile, the alkali addition removes the  $\text{Ca}^{2+}$  and  $\text{Mg}^{2+}$  with only  $\text{Cl}^-$  remaining.


To facilitate the direct alkaline seawater electrolysis in AE, the majority of previous research concentrated on the isolation of  $\text{Cl}^-$  from anode catalysts to realize a  $\text{Cl}^-$ -free

[\*] H. Liu,<sup>+</sup> Dr. H. Jin, J. Xu, Prof. Y. Zheng, Prof. S.-Z. Qiao  
 School of Chemical Engineering and Advanced Materials,  
 The University of Adelaide  
 5005 Adelaide, SA (Australia)  
 E-mail: yao.zheng01@adelaide.edu.au  
 s.qiao@adelaide.edu.au

Prof. J. Dong  
 Beijing Synchrotron Radiation Facility, Institute of High Energy  
 Physics, Chinese Academy of Sciences  
 100049 Beijing (China)  
 E-mail: dongjc@ihep.ac.cn

W. Shen,<sup>+</sup> Prof. P. Xi  
 College of Chemistry and Chemical Engineering,  
 Lanzhou University  
 730000 Lanzhou (China)

[<sup>+</sup>] These authors contributed equally to this work.

 © 2023 The Authors. Angewandte Chemie International Edition published by Wiley-VCH GmbH. This is an open access article under the terms of the Creative Commons Attribution License, which permits use, distribution and reproduction in any medium, provided the original work is properly cited.

water splitting, which can inhibit the possible corrosion and side reaction mentioned above.<sup>[19,20]</sup> This includes the construction of protective layers that stop the penetration of  $\text{Cl}^-$  or the design of an anion-rich surface for a catalyst that repels the  $\text{Cl}^-$  via electrostatic force.<sup>[21]</sup> These methods are essentially designed to achieve analogous alkaline pure water electrolysis but use alkaline seawater as feedstock. However, such rejection strategies are faced with the issue of unsatisfactory durability because the modified layer is usually not stable enough under harsh operating conditions.<sup>[22]</sup> To develop a high-performance catalyst for alkaline seawater splitting, the role of  $\text{Cl}^-$  needs to be clarified. Due to the complexity of the OER involving  $\text{Cl}^-$  at the interface between electrode and electrolyte, it is still challenging to determine how the  $\text{Cl}^-$  interacts with the active sites of the anode catalysts precisely.<sup>[23]</sup> In addition to  $\text{Cl}^-$ -related issues, the durability of high-activity catalysts themselves, e.g. layer double hydroxide (LDH) catalysts, is also a huge challenge when running in a high-concentration alkaline electrolyte. The reason is that the high activity is usually contributed by high metal valence states, which can in turn cause metal leaching and performance degradation under a high voltage operation.<sup>[24]</sup>

Herein, for the first time, we constructed an industrial-scale AE for alkaline seawater splitting by utilizing the adsorption of  $\text{Cl}^-$  from alkaline seawater feedstock on the surface of catalyst. Different from the well-known view that  $\text{Cl}^-$  is harmful to the catalyst, we demonstrate that  $\text{Cl}^-$  is advantageous to the OER activity and stability of NiFe LDH. In situ spectroscopic experiments demonstrate that  $\text{Cl}^-$  adsorption on Fe site can increase the Ni valence, as well as lower the Fe valence and stabilize the lattice oxygen during OER process. The former function results in a high OER activity (254 mV overpotential for  $100 \text{ mA cm}^{-2}$  current density) to outperform most catalysts and the latter enables NiFe LDH's great stability in alkaline seawater (over 300 h at  $200 \text{ mA cm}^{-2}$ ) in a three-electrode configuration. Owing to promoting effects of  $\text{Cl}^-$ , the industrial-scale alkaline seawater electrolyser, taking NiFe LDH as the anode, decreases the electricity consumption from  $5.95 \text{ kWh Nm}^{-3}$  (commercial purified water-based AE) to  $4.72 \text{ kWh Nm}^{-3}$  (saving 20.7 % electricity). In addition to its improved energy efficiency, this alkaline seawater-based AE performs exceptional durability for over 100 h at the current density of  $200 \text{ mA cm}^{-2}$ .

## Results and Discussion

### OER activity comparison in three-electrode configuration

Figure 1 shows the linear sweep voltammetry (LSV) and cyclic voltammetry (CV) curves of NiFe LDH (Figure S3 and S4) and another typical OER catalyst  $\text{Ni(OH)}_2$  running in two different electrolytes. They are 1 M KOH dissolved in deionized (DI) water (denoted as alkaline pure water) and natural seawater (collected from Henley Beach, SA, Australia, denoted as alkaline seawater). The pre-treatment process of natural seawater by KOH can be found in

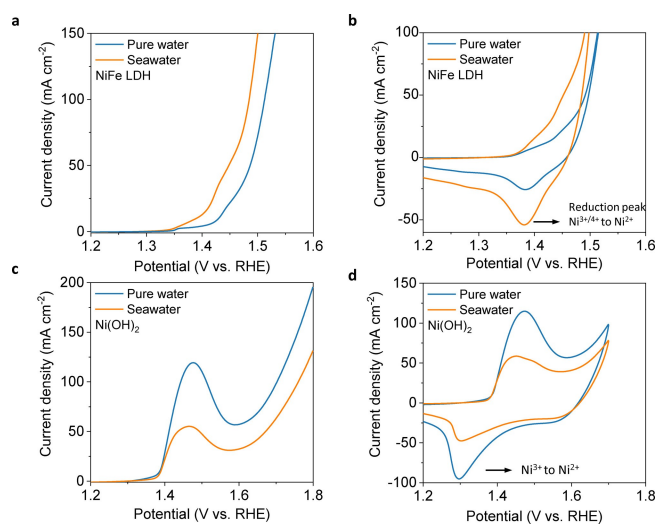


**Figure 1.** Electrochemical activity evaluation in alkaline pure water and alkaline seawater in three-electrode configuration. (a) LSV curves and (b) CV curves of NiFe LDH. (c) LSV curves and (d) CV curves of  $\text{Ni(OH)}_2$ .

experimental section (Figure S5). As shown in Figure 1a, The NiFe LDH tested in alkaline seawater performs better OER activity than that in alkaline pure water. Only 254 mV of overpotential is needed to achieve  $100 \text{ mA cm}^{-2}$ , which outperforms most catalysts for OER in alkaline pure water (Figure S7c). This increase can be rationalized by the formation of more high valence Ni species in alkaline seawater (Figure 1b). The similar phenomenon can be observed in simulated alkaline seawater (1 M KOH + 0.5 M NaCl, Figure S6, S7a). However, for  $\text{Ni(OH)}_2$  without a Fe promoter,  $\text{Cl}^-$  involvement results in an opposite activation effect. The LSV curves show that  $\text{Ni(OH)}_2$  possesses worse OER activity in alkaline seawater than in alkaline pure water because the formation of high valence Ni is inhibited in the former (Figure 1c, d, Figure S7b, S8). In addition, the analogous NiCo LDH also delivers better OER performance with more high-valence Ni/Co species in alkaline seawater (Figure S9).

### Structure evolution with $\text{Cl}^-$ interaction

In situ Raman spectroscopy analysis was conducted to determine the origin of activity enhancement of NiFe LDH in alkaline seawater (Figure S10, S11). Under 1.35 V, the NiFe LDH catalysts immersed in two electrolytes share the same weak peaks at  $461 \text{ cm}^{-1}$  and strong peaks at  $535 \text{ cm}^{-1}$ , which are assigned to the  $e_g$  bending mode and  $A_{1g}$  stretching modes of  $\text{Ni(OH)}_2$ .<sup>[25]</sup> For NiFe LDH measured in alkaline pure water, as the anodic potential rises to 1.4 V, the new peaks at  $477 \text{ cm}^{-1}$  and  $556 \text{ cm}^{-1}$  replace the initial two peaks (Figure 2a). The pair of those new peaks can be assigned to NiOOH, indicating the phase transition from  $\alpha$ -NiFe LDH to  $\gamma$ -NiFeOOH, which is accompanied by the valence increase from  $\text{Ni}^{2+}$  to  $\text{Ni}^{3+/4+}$ . In comparison, an early appearance of  $\alpha/\gamma$  transition was observed in alkaline

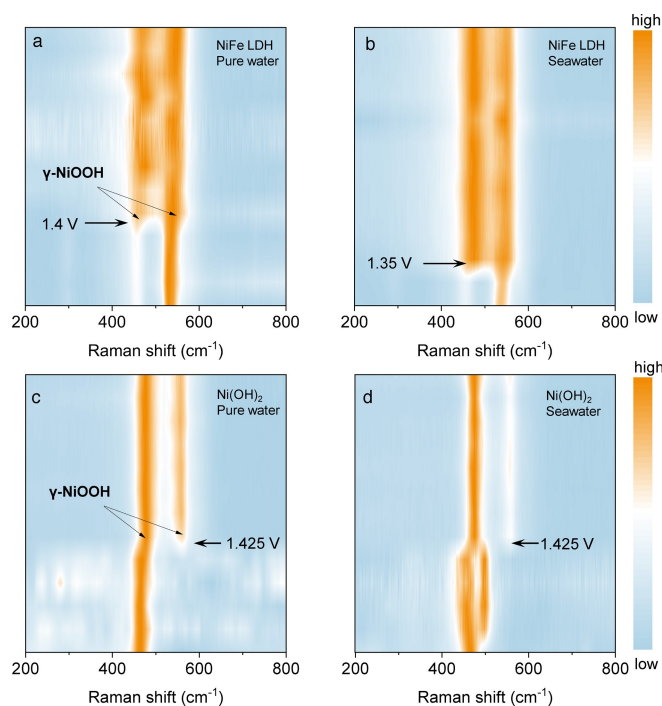


**Figure 2.** In situ Raman contour map. (a, b) NiFe LDH measured in (a) alkaline pure water and (b) alkaline seawater. (c, d) Ni(OH)<sub>2</sub> measured in (c) alkaline pure water and (d) alkaline seawater. Applied potentials range from 1.3 V to 1.6 V with an interval of 25 mV.

seawater (e.g., 1.35 V, Figure 2b), agreeing well with the results obtained from CV tests that the addition of Cl<sup>-</sup> facilitates the enhancement of Ni valence.

As for Ni(OH)<sub>2</sub>, the characteristic peaks of γ-NiOOH cannot be observed until voltages reach 1.425 V no matter in alkaline pure water or alkaline seawater (Figure 2c and 2d). The different α/γ transition behaviors of NiFe LDH and Ni(OH)<sub>2</sub> strongly indicate both Fe and Cl<sup>-</sup> are necessary to facilitate the formation of the active γ-phase during the OER process.

### Atomic evolution with Cl<sup>-</sup> interaction

To track the differences of catalyst's atomic evolution in alkaline pure water and alkaline seawater under OER conditions, in situ X-ray absorption spectroscopy (XAS) analysis was conducted. Ni and Fe's valence evolutions as a function of applied potentials are illustrated by summarizing the X-ray absorption near edge structure (XANES) energy shifts with three reaction stages (Figure 3a, Figure S12, S13). From open circuit potential to 1.1 V (initial stage), the Fe and Ni K-edge shifts in the two electrolytes share a similar trend. Then, the Fe K-edge shifts keep rising slowly between 1.1 V and 1.45 V (pre-catalytic stage), while the Ni K-edge shift moves to a more positive value in alkaline seawater than in alkaline pure water. However, when the potential reaches 1.6 V (OER stage), the Fe K-edge shift measured in alkaline seawater abnormally moves backward (decreasing to 0.45 eV), while the Fe K-edge shift keeps rising in

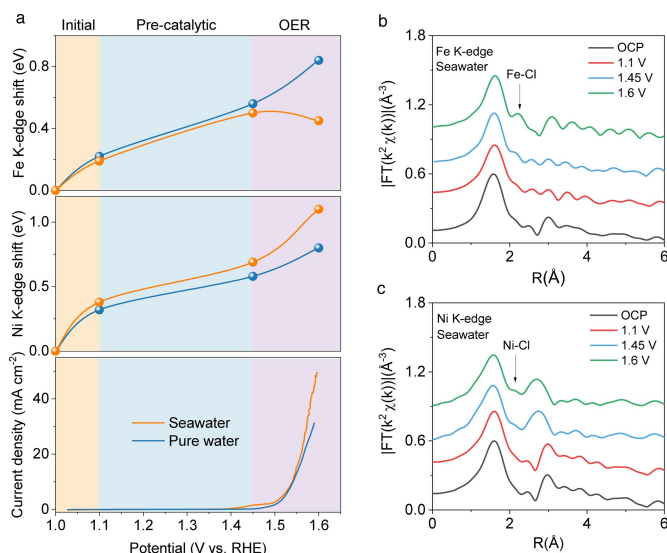


**Figure 3.** In situ XAS measurements using pristine NiFe LDH. (a) Shifts in the Fe and Ni K-edge position extracted from in situ XANES spectra and corresponding OER currents. (b, c) The k<sup>2</sup>-weighted FT-EXAFS spectra for (b) Fe K-edge and (c) Ni K-edge in alkaline seawater.

alkaline pure water as expected. Contrary to Fe, the Ni K-edge shift reaches the maximum value in alkaline seawater at 1.6 V, higher than that measured in alkaline pure water. This further indicates that Cl<sup>-</sup> stabilizes the valence state of Fe and raises the valence state of Ni.

In k<sup>3</sup>-weighted Fourier transformed extended X-ray absorption fine structure (FT-EXAFS) spectra (Figure 3b), a clear Fe–Cl peak can be observed in alkaline seawater after the potential reaches 1.45 V, which indicates the adsorption of Cl<sup>-</sup> species on the Fe site. However, no significant peak of Ni–Cl can be observed at all applied potentials (Figure 3c, Figure S14). This specific adsorption of Cl<sup>-</sup> on the Fe site, not Ni, is responsible for the opposite valence evolution trends for them revealed by XANES, which can be explained by the classic Pearson's hard-soft acid-base (HSAB) principle. It has been demonstrated that the Ni valence will increase to Ni<sup>4+</sup> for NiFe LDH under OER conditions, which is a harder Lewis acid than Fe<sup>3+</sup> site.<sup>[26,27]</sup> According to HSAB principle, harder acid tends to bind with harder base. In this way, Ni<sup>4+</sup> prefers to bind with OH<sup>-</sup> and Fe<sup>3+</sup> prefers to bind with Cl<sup>-</sup> because the OH<sup>-</sup> is a harder base than Cl<sup>-</sup>. In turn, the unique adsorption of Cl<sup>-</sup> on Fe<sup>3+</sup> stabilizes the oxidation state of Fe beyond the attack of OH<sup>-</sup>. Considering that Fe with high valence unavoidably leads to its dissolution for NiFe LDH operated in alkaline pure water,<sup>[28]</sup> a low oxidation state of Fe in alkaline seawater probably is beneficial for its OER stability.

### OER stability comparison in alkaline pure water and alkaline seawater

As widely recognized, Fe leaching is the major reason for the poor durability of NiFe LDH.<sup>[29]</sup> The OER stabilities of

the NiFe LDH catalysts in two electrolytes were then evaluated and compared using chronopotentiometry (Figure 4a). In 300 h running, the NiFe LDH catalyst measured in alkaline seawater affords unexpectedly better OER stability with a 53 mV potential increase than that in alkaline pure water (300 mV, Figure 4b), verifying the positive effect of  $\text{Cl}^-$  on OER stability. The concentrations of dissolved metal ions in different electrolytes were then detected by inductively coupled plasma mass spectrometry (ICP-MS).<sup>[30]</sup> As compared in Figure 4c, the minimum amount of dissolved Ni ( $140.3 \text{ ng mL}^{-1}$ ) and Fe ions ( $35.15 \text{ ng mL}^{-1}$ ) are found in alkaline seawater, which is lower than that tested in alkaline pure water. Besides, the ratio of Ni: Fe remains similar after the stability test in alkaline seawater, but this value increases from 2.82 to 3.25 in alkaline pure water, indicating a severe dissolution of Fe in the latter (Figure S15). Hence, based on the X-ray photoelectron spectroscopy (XPS) results of Ni 2p (Figure 4d, e), the reduced leaching of Fe allowed a greater amount of  $\text{Ni}^{3+}$  (857.6 eV,  $\text{Ni } 2p_{3/2}$ ) to retain after the test (constituting 28%), consequently ensuring superior durability performance in alkaline seawater. Additionally, the XPS spectra of O 1s for NiFe LDH and Ni 2p for  $\text{Ni}(\text{OH})_2$  are presented in Figure S16 for reference. The high-angle annular dark-field scanning transmission electron microscopy (HAADF-STEM) image and energy dispersive X-ray spectroscopy (EDS) elemental mapping also show the even distribution of Fe in NiFe LDH after running in alkaline seawater and pure water (Figure S17, S18). Taking structural evolution and

ICP-MS results together, we can confirm that the adsorption of  $\text{Cl}^-$  keeps the Fe in a low valence, inhibiting the leaching of Fe, thus achieving stable long-term OER durability.

### OER mechanism investigation

To bridge the remarkable OER performance and unique function of  $\text{Cl}^-$  on NiFe LDH, the OER mechanism in alkaline seawater was studied. In the alkaline pure water-based electrolyte, it has been widely known that NiFe LDH's lattice oxygen directly takes part in the formation of  $\text{O}_2$ , which is known as the so-called lattice oxygen mechanism (LOM).<sup>[31]</sup> Accordingly,  $^{18}\text{O}$  isotope-labeling experiments were conducted using in situ differential electrochemical mass spectrometry (DEMS) to quantify the activity of lattice oxygen. The NiFe LDH catalyst was first labeled with  $^{18}\text{O}$  isotopes via CV activation in  $\text{H}_2^{18}\text{O}$ -based 1 M KOH electrolyte. Subsequently, the  $^{18}\text{O}$  labeled catalysts were washed with  $\text{H}_2^{16}\text{O}$  three times to collect the real-time signals of  $m/z = 32$  ( $^{16}\text{O}_2$ ),  $m/z = 34$  ( $^{16}\text{O}^{18}\text{O}$ ), and  $m/z = 36$  ( $^{18}\text{O}_2$ ) during the CV measurements (Figure S19). Then the DEMS signals and CV curves are integrated to the mass spectrometric cyclic voltammograms (MSCVs). The MSCVs signals of  $^{16}\text{O}^{18}\text{O}$  and  $^{18}\text{O}_2$  are normalized by the content of  $^{16}\text{O}_2$ , with the ordinate representing their ratio. As shown in Figure 5a, b and Figure S20,  $^{18}\text{O}$  labeled NiFe LDH delivers more than three times as high contents of  $^{16}\text{O}^{18}\text{O}$  and  $^{18}\text{O}_2$  in alkaline pure water as that measured in alkaline seawater, indicating that the participation of lattice oxygen is suppressed in the latter. In addition, the less activity dependence on pH in alkaline seawater than in alkaline pure water also demonstrates that the activity of lattice oxygen is reduced by  $\text{Cl}^-$  adsorption (Figure S21). Such less active lattice oxygen can also explain the excellent durability of NiFe LDH in alkaline seawater because the active lattice oxygen usually leads to the instability of crystal structure.<sup>[32,33]</sup>

It should be noted that the stabilized lattice oxygen cannot explain the enhanced OER activity in alkaline seawater as the LOM is inhibited. Besides LOM, another OER mechanism is described as the adsorbate evolution mechanism (AEM), which normally shows less activity than LOM. In situ attenuated total reflectance surface-enhanced infrared absorption spectroscopy (ATR-SEIRAS) was employed to investigate the participation of AEM by identifying the intensities of surface adsorbed OOH (\*OOH) intermediate (Figure 5c, d).<sup>[34]</sup> It is clear that the intensities of \*OOH in alkaline seawater exceed that in alkaline pure water at all applied potentials, suggesting higher \*OOH coverage (Figure 5e). Namely, although the LOM is suppressed, the AEM is facilitated for OER operated in alkaline seawater, which accounts for the enhanced activity.

Based on the electrochemical tests and a series of in situ spectroscopic measurements, we propose a  $\text{Cl}^-$  boosted OER process in alkaline seawater, including the atomic valence evolution, structural evolution and mechanism transfer (Figure 5f). In alkaline pure water, as the anodic potential rises, the valences of Ni and Fe increase to  $\text{Ni}^{3+}$

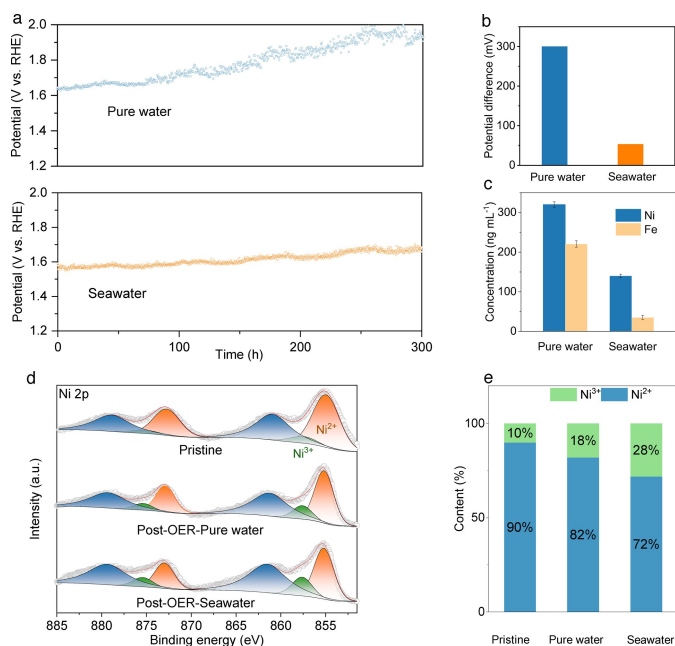


**Figure 4.** OER durability measurements. (a) OER stability test at a constant current density of  $200 \text{ mA cm}^{-2}$  for NiFe LDH in two electrolytes. (b) Potential differences at the start and the end of the stability test. (c) Concentrations of dissolved Ni and Fe ions after stability test determined by ICP-MS. (d) Ni 2p XPS spectra for NiFe LDH before and after stability test. (e) Peak area ratio of  $\text{Ni}^{3+}/\text{Ni}^{2+}$  obtained from XPS results.

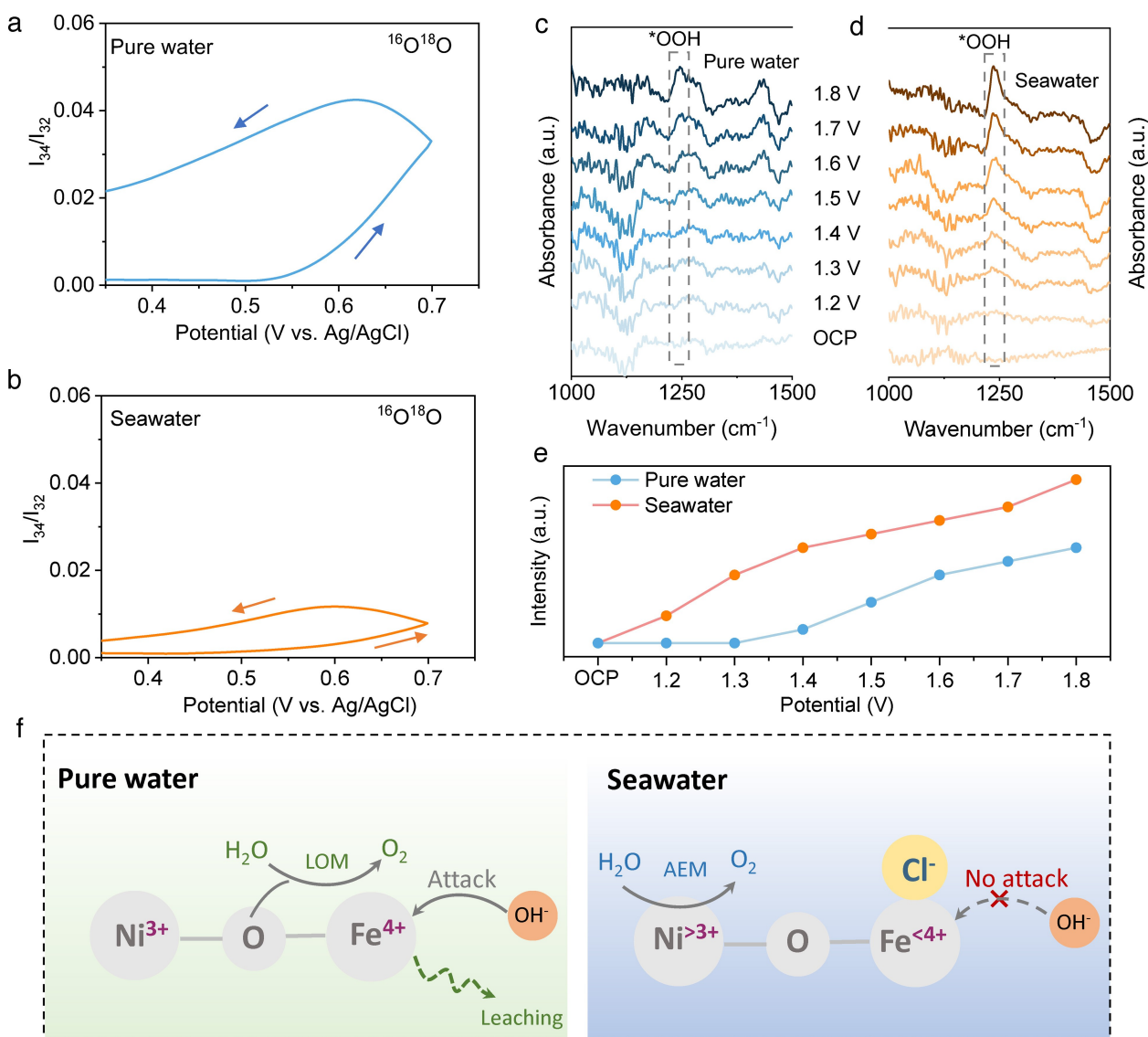


**Figure 5.** OER mechanism investigation. (a, b) MSCVs signals of  $^{16}\text{O}^{18}\text{O}$  content from DEMS test on  $^{18}\text{O}$  labeled NiFe LDH in (a) alkaline pure water and (b) alkaline seawater. (c, d) In situ ATR-SEIRAS spectra of NiFe LDH in (c) alkaline pure water and (d) alkaline seawater. (e) Coverage of  $^*\text{OOH}$  as a function of applied potentials. (f) Schematic illustration for structure evolution and OER mechanism transfer in alkaline pure water and alkaline seawater.

and  $\text{Fe}^{4+}$  with the OER proceeding via a LOM pathway.  $\text{OH}^-$  attack happens (possible) because of the increase in Fe valence after the anodic potential increment. As the Fe valence is increased at high potential, it becomes a relatively hard acid and is attacked by hard base  $\text{OH}^-$ , which leads to its leaching and results in unsatisfactory durability. In alkaline seawater, due to the  $\text{Cl}^-$  adsorption on the Fe site, the Fe is protected from the attack of  $\text{OH}^-$ , thus suppressing its leaching. Simultaneously, Ni valence is increased, with the AEM pathway dominating the OER. The improvement of Ni valence and promoted AEM explains the activity increase in alkaline seawater. The protective effect of  $\text{Cl}^-$  on Fe and the resultant suppression of Fe leaching, along with the stable lattice oxygen aid the excellent stability performance.

#### H-cell and commercial AE device performance

The overall alkaline seawater-splitting performances were eventually evaluated in an H-cell (electrode area:  $1\text{ cm}^2$ ) and a commercial AE (electrode area:  $120\text{ cm}^2$ ). The NiFe LDH and  $\text{NiS}_x$  were used as the anode and cathode electrodes, respectively.<sup>[35]</sup> The hydrogen evolution reaction (HER) activity of  $\text{NiS}_x$  is shown in Figure S22. For H-cell measurement, as expected, better overall electrochemical activity and durability are obtained in alkaline seawater than in alkaline pure water (Figure 6a, b). As a comparison,  $\text{Ni}(\text{OH})_2$  shows a much worse activity and undergoes a quick decline of stability in alkaline seawater because there is no such  $\text{Cl}^-$  promotion and protection mechanism. Additionally, the participation of CIER was investigated by quantifying the amounts of  $\text{O}_2$  generated in two electrolytes (Fig-

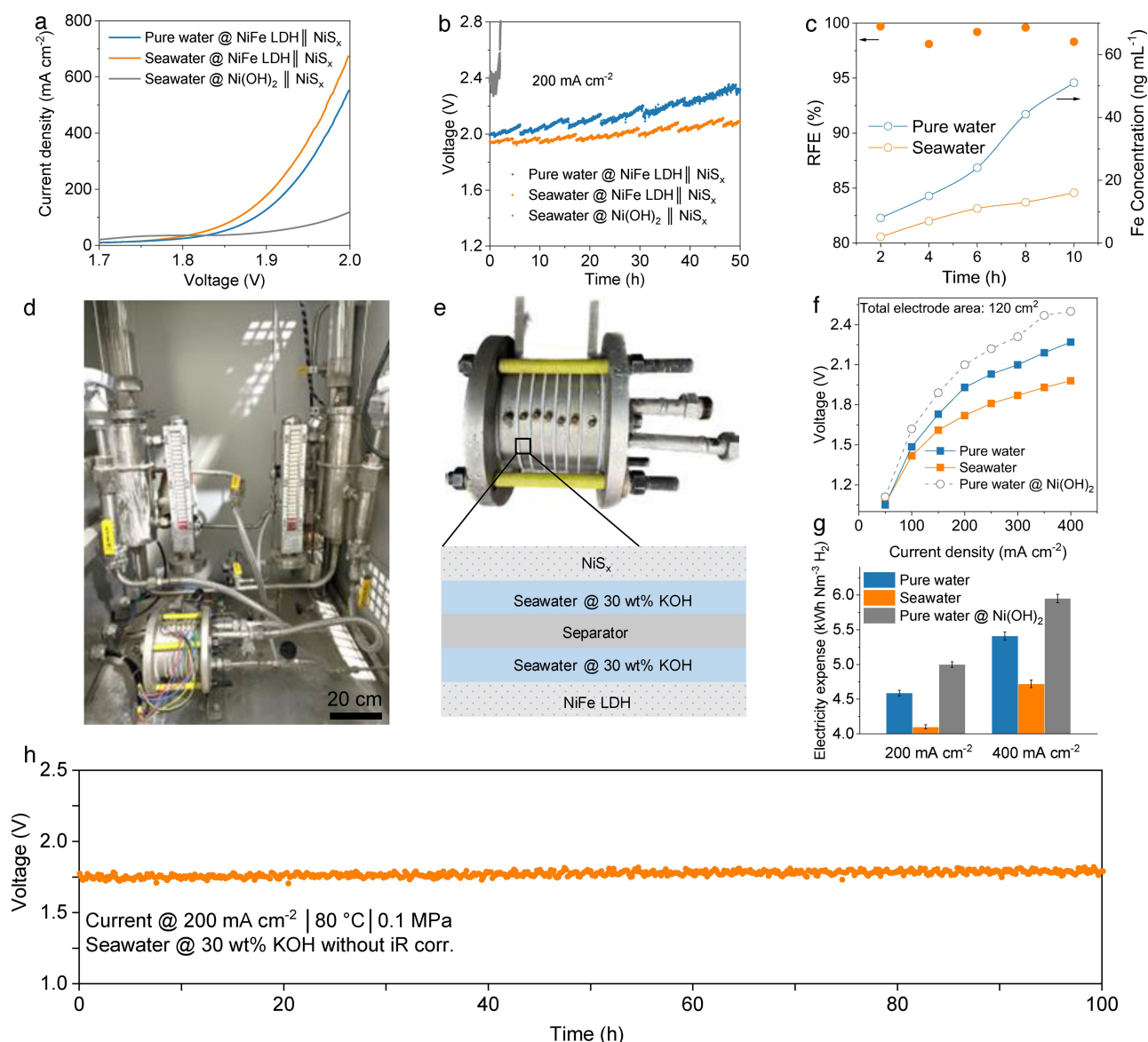


**Figure 6.** Evaluation of overall water splitting performance in two-electrode configuration and scale-up test in a commercial AE. Overall water splitting performance in two-electrode configuration for (a) activity, (b) durability (at  $200 \text{ mA cm}^{-2}$ ) and (c) corresponding RFE (left ordinate) and dissolution of Fe (right ordinate) during durability test. (d) Optical image of the commercial AE. (e) Enlarged view of the electrolyser and schematic illustration of an electrolyser cell. (f) Polarization curves of AE using alkaline pure water and alkaline seawater at  $80^\circ\text{C}$ . (g) A comparison of electricity expense for AE calculated from polarization curves. (h) Durability test for the commercial AE at a constant current density of  $200 \text{ mA cm}^{-2}$ .

ure S23). The RFE in alkaline seawater at  $200 \text{ mA cm}^{-2}$  operation is close to 100% without CIER, indicating that a  $\text{Cl}^-$ -free alkaline seawater splitting is achieved (Figure 6c). As a key metric for evaluating durability, the leaching of Fe was reduced by more than half, from  $51 \text{ ng mL}^{-1}$  to  $16 \text{ ng mL}^{-1}$  at the end of the test (Figure 6c). Afterward, to investigate the viability of our strategy for large-scale direct alkaline seawater electrolysis, a commercial AE was fabricated running at  $80^\circ\text{C}$  (Figure 6d, e). As reported, the performance of alkaline seawater electrolysis is far inferior to that of alkaline pure water electrolysis, as also evidenced in using  $\text{Ni(OH)}_2$  anode in H-cell (Figure 6a).<sup>[36]</sup> However, in our scale-up system, the advantageous interactions between

both  $\text{Cl}^-$  and NiFe LDH have compensated for these negative effects. The polarization curves (without iR compensation) in Figure 6f show that alkaline seawater-based industrial-scale AE has improved water electrolysis activity compared with that using alkaline pure water. As a result, when using highly active NiFe LDH, the electricity expense of  $\text{H}_2$  production decreased from  $4.59 \text{ kWh Nm}^{-3} \text{ H}_2$  to  $4.1 \text{ kWh Nm}^{-3} \text{ H}_2$  at  $200 \text{ mA cm}^{-2}$  operation current density and from  $5.41 \text{ kWh Nm}^{-3} \text{ H}_2$  to  $4.72 \text{ kWh Nm}^{-3} \text{ H}_2$  at  $400 \text{ mA cm}^{-2}$  from alkaline pure water to alkaline seawater running (Figure 6g). As a comparison, these values on a commercial  $\text{Ni(OH)}_2$ -based alkaline pure water AE are 5 kWh and 5.95 kWh, respectively (Figure 6g). This means

the alkaline seawater electrolysis with NiFe LDH anode decreases the electricity expense by 12.8% to the alkaline pure water electrolysis with same anode and 20.7% to the commercial alkaline pure water electrolysis. Moreover, at a constant current density of 200 mA cm<sup>-2</sup> or 500 mA cm<sup>-2</sup>, the industrial-scale AE with NiFe LDH works stably for over 100 h and 40 h, respectively, with no obvious failure for alkaline seawater electrolysis (Figure 6h and Figure S24).

## Conclusion

In summary, we have achieved direct and CIER-free alkaline seawater electrolysis in a NiFe LDH-based commercial AE, which saves up to 12.8% and 20.7% of the electricity compared to the conventional purified water-based AE with the same anode and the commercial Ni(OH)<sub>2</sub> anode, respectively. The key to its greatly increased performance is the utilization of the positive synergies between Cl<sup>-</sup> and NiFe LDH. Via electrochemical tests and a set of in situ spectroscopic measurements (Raman, XAS, ATR-SEIRAS, DEMS), it was found that the specific adsorption behavior of Cl<sup>-</sup> in alkaline seawater contributes to the OER activity and stability enhancement for NiFe LDH by triggering the transition of OER mechanism from LOM to AEM. Our findings not only provide a new and comprehensive understanding of the impact of Cl<sup>-</sup> on typical OER catalysts, but also offer important guidance for the design of catalyst for electrocatalytic reaction occurring in seawater.

## Acknowledgements

The authors gratefully acknowledge the financial support provided by the Australian Research Council through Discovery Project Programs (FL170100154, FT200100062, DP230102027, DP220102596, and DP190103472). J.D. acknowledges financial support from the Youth Innovation Promotion Association of the Chinese Academy of Sciences (Y2022006). XAS measurements were undertaken at Beijing Synchrotron Radiation Facility (BSRF). Open Access publishing facilitated by The University of Adelaide, as part of the Wiley - The University of Adelaide agreement via the Council of Australian University Librarians.

## Conflict of Interest

Inventive aspects of this publication have been included in a provisional patent application.

## Data Availability Statement

The data that support the findings of this study are available from the corresponding author upon reasonable request.

**Keywords:** Alkaline Water Electrolyser · Chloride Adsorption · NiFe LDH · Oxygen Evolution Reaction · Seawater Electrolysis

- [1] L. Wan, M. Pang, J. Le, Z. Xu, H. Zhou, *Nat. Commun.* **2022**, *13*, 7956.
- [2] Q. Xu, L. Zhang, J. Zhang, J. Wang, Y. Hu, H. Jiang, C. Li, *EnergyChem* **2022**, *4*, 100087.
- [3] K. Zeng, D. Zhang, *Prog. Energy Combust. Sci.* **2010**, *36*, 307–326.
- [4] S. Dresp, F. Dionigi, M. Klingenhof, P. Strasser, *ACS Energy Lett.* **2019**, *4*, 933–942.
- [5] H. Jin, X. Wang, C. Tang, A. Vasileff, L. Li, A. Slattery, S. Z. Qiao, *Adv. Mater.* **2021**, *33*, 2007508.
- [6] F. Dionigi, T. Reier, Z. Pawolek, M. Gliech, P. Strasser, *ChemSusChem* **2016**, *9*, 962–972.
- [7] R. K. B. Karlsson, A. Cornell, *Chem. Rev.* **2016**, *116*, 2982–3028.
- [8] S. Zhang, L. Hou, H. Du, H. Wei, B. Liu, Y. Wei, *Corros. Sci.* **2020**, *167*, 108531.
- [9] Y. Zheng, S. Z. Qiao, *Joule* **2023**, *7*, 20–22.
- [10] P. Farràs, P. Strasser, A. J. Cowan, *Joule* **2021**, *5*, 1921–1923.
- [11] C. He, Z. Liu, J. Wu, X. Pan, Z. Fang, J. Li, B. A. Bryan, *Nat. Commun.* **2021**, *12*, 4667.
- [12] Y. Kuang, M. J. Kenney, Y. Meng, W. H. Hung, Y. Liu, J. E. Huang, R. Prasanna, P. Li, Y. Li, L. Wang, M. C. Lin, M. D. McGehee, X. Sun, H. Dai, *Proc. Natl. Acad. Sci. USA* **2019**, *116*, 6624–6629.
- [13] L. Yu, Q. Zhu, S. Song, B. McElhenny, D. Wang, C. Wu, Z. Qin, J. Bao, Y. Yu, S. Chen, Z. Ren, *Nat. Commun.* **2019**, *10*, 5106.
- [14] J. Guo, Y. Zheng, Z. Hu, C. Zheng, J. Mao, K. Du, M. Jaroniec, S.-Z. Qiao, T. Ling, *Nat. Energy* **2023**, *8*, 264–272.
- [15] J. G. Vos, Z. Liu, F. D. Speck, N. Perini, W. Fu, S. Cherevko, M. T. M. Koper, *ACS Catal.* **2019**, *9*, 8561–8574.
- [16] S. Dresp, F. Dionigi, S. Loos, J. Ferreira de Araujo, C. Spöri, M. Gliech, H. Dau, P. Strasser, *Adv. Energy Mater.* **2018**, *8*, 1800338.
- [17] S. Dresp, T. Ngo Thanh, M. Klingenhof, S. Brückner, P. Hauke, P. Strasser, *Energy Environ. Sci.* **2020**, *13*, 1725–1729.
- [18] M. Klingenhof, P. Hauke, M. Kroschel, X. Wang, T. Merzdorf, C. Binnering, T. N. Thanh, B. Paul, D. Teschner, R. Schl, P. Strasser, *ACS Energy Lett.* **2022**, *7*, 3415–3422.
- [19] J. Chang, G. Wang, Z. Yang, B. Li, Q. Wang, R. Kuliiev, N. Orlovskaya, M. Gu, Y. Du, G. Wang, Y. Yang, *Adv. Mater.* **2021**, *33*, 2101425.
- [20] L. Yu, L. Wu, B. McElhenny, S. Song, D. Luo, F. Zhang, Y. Yu, S. Chen, Z. Ren, *Energy Environ. Sci.* **2020**, *13*, 3439–3445.
- [21] K. Obata, K. Takanabe, *Angew. Chem. Int. Ed.* **2018**, *57*, 1616–1620.
- [22] W. Tong, M. Forster, F. Dionigi, S. Dresp, R. Sadeghi Erami, P. Strasser, A. J. Cowan, P. Farràs, *Nat. Energy* **2020**, *5*, 367–377.
- [23] S. Dresp, F. Dionigi, M. Klingenhof, T. Merzdorf, H. Schmies, J. Drnec, A. Poulain, P. Strasser, *ACS Catal.* **2021**, *11*, 6800–6809.
- [24] C. Feng, F. Wang, Z. Liu, M. Nakabayashi, Y. Xiao, Q. Zeng, J. Fu, Q. Wu, C. Cui, Y. Han, N. Shibata, K. Domen, I. D. Sharp, Y. Li, *Nat. Commun.* **2021**, *12*, 5980.
- [25] S. Lee, L. Bai, X. Hu, *Angew. Chem. Int. Ed.* **2020**, *59*, 8072–8077.
- [26] M. Liu, K. A. Min, B. Han, L. Y. S. Lee, *Adv. Energy Mater.* **2021**, *11*, 2101281.
- [27] Q. Tu, W. Liu, M. Jiang, W. Wang, Q. Kang, P. Wang, W. Zhou, F. Zhou, *ACS Appl. Energy Mater.* **2021**, *4*, 4630–4637.
- [28] S. Anantharaj, S. Kundu, S. Noda, *Nano Energy* **2021**, *80*, 105514.

- [29] D. Y. Chung, P. P. Lopes, P. Farinazzo Bergamo Dias Martins, H. He, T. Kawaguchi, P. Zapol, H. You, D. Tripkovic, D. Strmcnik, Y. Zhu, S. Seifert, S. Lee, V. R. Stamenkovic, N. M. Markovic, *Nat. Energy* **2020**, *5*, 222–230.
- [30] R. Chen, S. F. Hung, D. Zhou, J. Gao, C. Yang, H. Tao, H. Bin Yang, L. Zhang, L. Zhang, Q. Xiong, H. M. Chen, B. Liu, *Adv. Mater.* **2019**, *31*, 1903909.
- [31] Z. He, J. Zhang, Z. Gong, H. Lei, D. Zhou, N. Zhang, W. Mai, S. Zhao, Y. Chen, *Nat. Commun.* **2022**, *13*, 2191.
- [32] Z. Y. Wu, F. Y. Chen, B. Li, S. W. Yu, Y. Z. Finrock, D. M. Meira, Q. Q. Yan, P. Zhu, M. X. Chen, T. W. Song, Z. Yin, H. W. Liang, S. Zhang, G. Wang, H. Wang, *Nat. Mater.* **2023**, *22*, 100–108.
- [33] Y. Wen, P. Chen, L. Wang, S. Li, Z. Wang, J. Abed, X. Mao, Y. Min, C. T. Dinh, P. De Luna, R. Huang, L. Zhang, L. Wang, L. Wang, R. J. Nielsen, H. Li, T. Zhuang, C. Ke, O. Voznyy, Y. Hu, Y. Li, W. A. Goddard, B. Zhang, H. Peng, E. H. Sargent, *J. Am. Chem. Soc.* **2021**, *143*, 6482–6490.
- [34] K. Du, L. Zhang, J. Shan, J. Guo, J. Mao, C. C. Yang, C. H. Wang, Z. Hu, T. Ling, *Nat. Commun.* **2022**, *13*, 5448.
- [35] J. Wang, Z. Zhang, H. Song, B. Zhang, J. Liu, X. Shai, L. Miao, *Adv. Funct. Mater.* **2021**, *31*, 2008578.
- [36] H. Xie, Z. Zhao, T. Liu, Y. Wu, C. Lan, W. Jiang, L. Zhu, Y. Wang, D. Yang, Z. Shao, *Nature* **2022**, *612*, 673–678.

Manuscript received: August 10, 2023

Accepted manuscript online: September 15, 2023

Version of record online: October 11, 2023